Four-vector correlation experiment on Ne($3p$)+He collisions: Measurements on intramultiplet mixing

S. S. Op de Beek, J. P. J. Driessen, K. H. J. M. Robben, H. C. W. Beijerinck, and B. J. Verhaar
Eindhoven University of Technology, P.O. Box 512, 5600 MB Eindhoven, The Netherlands
(Received 9 October 1996; revised manuscript received 8 May 1997)

Intramultiplet mixing collisions have been investigated using polarized Ne($3p$) atoms with a well-defined initial relative velocity, i.e., two initial-state vectors. By analyzing the final-state center-of-mass velocity with a (Doppler-detuned) probe laser with a well-defined polarization and detecting the laser-induced fluorescence we measure the differential cross section and the polarization of the final state, i.e., two final-state vectors. Measurements have been done at a collision energy $E=70$ meV, for both the α_7 and α_9 (Paschen numbering) initial states. For the elastic $\alpha_7 \rightarrow \alpha_7$ collisions the experimental results are strongly hindered by the undesired response on elastic scattering of the metastable Ne($3s,{}^3P_0$) state. Inelastic collisions have been investigated for the α_9 state, that forms a closed level system with the metastable Ne($3s,{}^3P_2$) state. For the $\alpha_9 \rightarrow \alpha_8$ transition experimental results are presented for both parallel and perpendicular orientations of the polarizations of the pump and probe laser, respectively, as well as for circular polarized (σ^+,σ^+) and (σ^+,σ^-) configurations. The experiments are compared to a full quantum-mechanical coupled channels calculation of the scattering process, using the model potentials of Hennecart and Masnou-Seeuws as input. The output of this calculation is combined with a density matrix description of the initial- and final-state polarization. Both shape of the differential cross sections and their relative scaling for different laser polarizarion configurations agree well with experiment. This gives strong support for the quality of the model potentials used.
[S1050-2947(97)08509-0]

PACS number(s): 34.50.Pi

I. INTRODUCTION

The study of alignment and orientation in atomic collisions has yielded an enormous wealth of detailed information on the mechanisms and dynamics of collisional excitation and energy transfer. Complete information requires additional detection of the polarization of the final state after the collision. In principle both atomic *alignment* (i.e., symmetric population of magnetic sublevels) and *orientation* (i.e., asymmetric population of magnetic substates) can be determined [1–10]. In favorable cases a complete set of collision amplitudes for the coherently excited atomic states, including their relative phases, can be derived [5]. Such a study brings experimental results much closer to a theoretical study, which may reveal important features of the potential curves [11–18].

Generally, experiments with a number n of controllable vector quantities such as relative velocity and alignment or orientation of atoms are called n-vector correlation measurements [2]. Polarized-atom collision experiments where the initial relative velocity and initial alignment or orientation are controlled are typical examples of two-vector experiments [19,20]. Combining these two-vector experiments with final-state analysis with respect to the alignment and/or final velocity results in three-vector [4–6] and four-vector [21] correlation experiments.

Many three- and four-vector correlation experiments have been performed for systems with an atom excited directly from the ground state, such as Na, Ba, and Ca, colliding with rare gases [4,5]. Because of the large experimental signals it is possible to resolve the final states with respect to final velocity or final orientation or alignment. A quantum-mechanical calculation is hard to perform for these systems since accurate potential information is very scarce.

The two-vector correlation experiment of the intramultiplet mixing process

$$\mathrm{Ne}(3p,\alpha_i)+\mathrm{He} \rightarrow \mathrm{Ne}(3p,\alpha_f)+\mathrm{He}+\Delta E \qquad (1)$$

has been studied in detail in the thermal [19] and superthermal [20] energy range. The short-lived initial Ne($3p,\alpha_i$) states ($\tau=20$ ns) are produced by laser excitation from one of the metastable Ne($3s$) states, ${}^3P_0$ or ${}^3P_2$, which account for an excited fraction $\eta \approx 10^{-5}$ of the total atomic beam flux. Therefore the densities of the initial Ne($3p$) states are much smaller compared to alkali-metal-atom densities available for excitation. By measuring the fluorescence intensity of a decay transition for both the initial and final state, polarized-atom cross sections $Q_{i\rightarrow f}^{|M_i|}$ can be determined [19,20]. Here M_i is the magnetic quantum number of the electronic angular momentum J of the initial state with respect to the initial relative velocity $\boldsymbol{v}_i$. Both a semiclassical and fully quantum-mechanical analysis result in theoretical cross sections which are in good agreement with the experimental data [19,20]. Although the experimental signals are rather small, the advantage of the system in Eq. (1) lies in the available accurate potential information [22–24], in contrast to the excited alkali-metal-atom ground-state noble gas systems.

In this paper we focus on a pump-probe experiment performed on the collision process of Eq. (1). The following pump-probe scheme is used:

$$\begin{array}{ccc} & & \mathrm{Ne}(4d)\rightarrow \mathrm{LIF}:\lambda_d \\ & & \uparrow(\lambda_{\mathrm{prb}}) \\ \mathrm{Ne}(3p,\alpha_i)+\mathrm{He} & \rightarrow & \mathrm{Ne}(3p,\alpha_f)+\mathrm{He} \\ \uparrow(\lambda_{\mathrm{pmp}}) & & \\ \mathrm{Ne}(3s,{}^3P_{0,2}), & & \end{array} \tag{2}$$

where the Ne($3p$) fine structure levels are denoted by the Paschen numbering ($i,f\in 1,\ldots,10$). The final state Ne($3p,\alpha_f$) is probed with a laser-induced fluorescence (LIF) technique which is combined with a Doppler probing scheme to resolve the final-state velocity. This pump-probe scheme has been chosen such that the decay fluorescence of the Ne($4d$) state ($\lambda_d\approx 530$ nm) is isolated from decay lines from other multiplets ($\lambda=580-670$ nm). Moreover, the decay lines of the Ne($4d$) state have large branching ratios ($>60\%$) which make them suitable for the LIF technique.

In this paper we focus on two types of scattering processes: (i) elastic collisions for $\alpha_7\rightarrow\alpha_7$ and (ii) inelastic collisions for $\alpha_9\rightarrow\alpha_8$. In principle, four vector parameters can be examined in the experiment; two velocity vectors, (1) $\boldsymbol{v}_i$ the initial relative velocity and (2) $\boldsymbol{v}_f$ the final relative velocity, of the colliding particles and two alignment or orientation vectors (3) $\boldsymbol{E}_{\mathrm{pmp}}$ the polarization vector of the pump laser used to prepare the initial state and (4) $\boldsymbol{E}_{\mathrm{prb}}$ the polarization vector of the probe laser used in the LIF detection scheme. In our crossed beam experiment the initial relative velocity $\boldsymbol{v}_i$ is well defined. The final velocity is detected through a Doppler detection scheme which is combined with the LIF scheme. Using polarization rotators the polarizations of both lasers can be controlled. The number of controllable parameters in this four-vector experiment can be very large. To limit the number of measurements we use fixed laser beam directions in our setup: the pump- and probe-laser beams are counterpropagating, perpendicular to the initial relative velocity $\boldsymbol{v}_i$.

In this paper we present experimental data on the final-state analysis of the intramultiplet mixing process in Eq. (1). On the basis of two processes, $\alpha_7\rightarrow\alpha_7$ and $\alpha_9\rightarrow\alpha_8$, we investigate the feasibility of a final-state analysis for short-lived Ne($3p$) states. Section II will deal with the final-state analysis where the LIF detetection scheme is combined with the Doppler probing technique. The experimental setup is described in Sec. III. In the same section the implementation of the pump and probe lasers is discussed. The Doppler probing technique is calibrated by applying it to elastic scattering of metastable Ne($3s$) states. The results of this calibration are presented in Sec. IV. In Secs. V and VI the four-vector experiments for elastic and inelastic scattering are discussed, respectively. In Sec. VII the experimental data are compared with theoretical simulations based on a fully quantum-mechanical coupled channels calculation. Finally, in Sec. IX concluding remarks are given.

II. FINAL-STATE ANALYSIS

A. LIF technique

Information about the final-state orientation and alignment is acquired using a LIF technique, which has been described in more detail by Smith *et al.* [5] for the Ca-He system. In our case, the second laser beam probes the final Ne($3p,\alpha_f$) state by exciting it to the Ne($4d$) level. From the decay fluorescence of the Ne($4d$) state information about the magnetic sublevel distribution for the final Ne($3p,\alpha_f$) state is obtained. The pump-probe scheme is depicted in Fig. 1. In this setup the initial Ne($3p,\alpha_i$) state is selected by the pump laser (λ_{pmp}); the wavelength of the probe laser (λ_{prb}) determines which final state is analyzed. We label the Ne($3p$) state with $|p\rangle$ and the state coupled by the probe laser by $|d\rangle$.

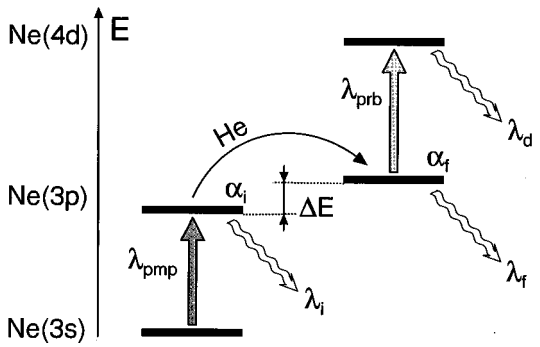

FIG. 1. Scheme of a general pump-probe experiment. The pump laser excites the Ne($3s$) state to the Ne($3p,\alpha_i$) state. The collision-induced final state Ne($3p,\alpha_f$) is probed by exciting it to a state in the Ne($4d$) multiplet with a probe laser and measuring the fluorescence at λ_d.

The final state has a total angular momentum qunatum number J in the range $0\leqslant J\leqslant 3$ for which different probing schemes are possible. In Fig. 2 we show the possible probing schemes for a $J=1$ final state with a linearly or circularly polarized probe laser. By saturating the probe transition, each of the probed magnetic sublevels of the final state is detected with equal probability. Obviously, the transition $J\rightarrow J+1$ probes all magnetic sublevels and cannot provide alignment or orientation information of the final state. However, using the $J\rightarrow J$ and $J\rightarrow J-1$ transitions, different subsets of magnetic sublevels are excited and combinations of these two probing schemes enable us to extract more information than either probing scheme separately. Using circularly polarized light, the asymmetry in the probed magnetic sublevel distribution gives information on the orientation of the final state.

In the configuration described in this paper the pump- and probe-laser beams are counter propagating, perpendicular to the initial relative velocity $\boldsymbol{v}_i$ as shown in Fig. 3. In the case

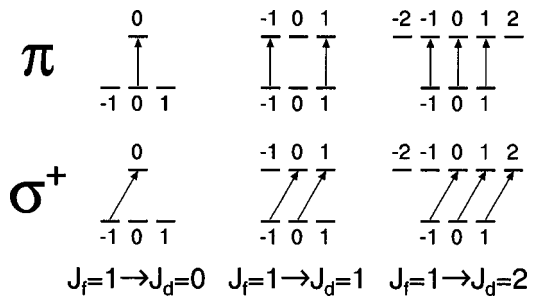

FIG. 2. Probe schemes for a $J_f=1$ final state for linearly polarized (π) and circularly polarized (σ) light, respectively. Only the schemes with $J_d\leqslant J_f$ give information on alignment and/or orientation.

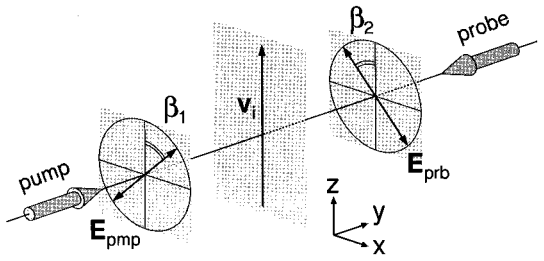

FIG. 3. The configuration of the linear laser polarizations. The polarization vectors $\boldsymbol{E}_{\rm pmp}$ and $\boldsymbol{E}_{\rm prb}$ of pump and probe lasers, respectively, are rotated over angles β_1 and β_2 in a plane perpendicular to the propagation direction of the lasers.

of linearly polarized laser beams the polarization angles β_1 and β_2, defined with respect to the initial relative velocity $\boldsymbol{v}_i$, can be varied using $\lambda/2$ plates. The linearly polarized configurations (β_1,β_2) that we investigate consist of a set of parallel polarizations: (0,0) and $(\pi/2,\pi/2)$ and a set of perpendicular polarizations: $(0,\pi/2)$ and $(\pi/2,0)$. In the case of circular polarization two configurations are possible: (σ^+,σ^+), (σ^+,σ^-). Combinations of linear and circular polarizations have not been investigated.

B. Doppler probing

The LIF probing scheme can be combined with a Doppler technique to resolve the velocity component of the final state in the probe-laser beam direction. The velocities of the Ne and He atoms are shown in a Newton diagram in Fig. 4 together with the initial relative velocity $\boldsymbol{v}_i$. The final velocity $\boldsymbol{u}_f$ of the Ne$(3p,\alpha_f)$ state in the center-of-mass (c.m.) system has an arbitrary direction resulting in the so-called (in)elastic scattering sphere centered around the c.m. velocity $\boldsymbol{v}_{\rm c.m.}$. The radius of the scattering sphere is given by

$$u_f=\frac{m_{\rm He}}{m_{\rm Ne}+m_{\rm He}}v_f, \tag{3}$$

with $\boldsymbol{v}_f$ being the final relative velocity. Depending on the sign of ΔE in Eq. (1) the radius is smaller than, equal to, or larger than the initial relative velocity u_i. In Fig. 4 the situation for an elastic collision is shown. The particles which are probed by the $\delta_{\rm prb}$-detuned laser beam have a well-defined velocity component with respect to the y-axis (laser beam axis). This results in the so-called ''Doppler cone'' with a top angle χ which depends on the laser detuning $\delta_{\rm prb}$ through the Doppler detuning

$$\delta_{\rm prb}=\boldsymbol{k}_{\rm prb}\cdot(\boldsymbol{v}_{\rm c.m.}+\boldsymbol{u}_f)=\Delta\omega_{\rm c.m.}+k_{\rm prb}u_f\cos(\chi), \tag{4}$$

with $\boldsymbol{k}_{\rm prb}$ being the wave vector of the probe laser beam. Here we have taken into account the transformation from the c.m. frame to the laboratory frame. The center-of-mass contribution $\Delta\omega_{\rm c.m.}$ is equal to zero because the laser beam is aligned perpendicular to the two atomic beams. The detuning $\delta_{\rm prb}$ and the angle χ are related by

$$\delta_{\rm prb}=k_{\rm prb}u_f\cos(\chi)=\Delta\omega_{\rm max}\cos(\chi). \tag{5}$$

The linewidth $\gamma_{\rm prb}$ of the probe laser and the natural linewidth $\Gamma_{\rm prb}$ of the probing transition result in a finite angular

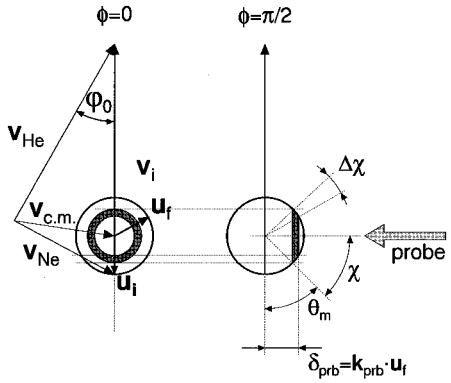

FIG. 4. Newton diagram for an elastic collision. The initial Ne velocity in the center-of-mass coordinate system is indicated by $\boldsymbol{u}_i$. The shaded ring represents the velocity class which is resonant with a laser with detuning $\delta_{\rm prb}$. The left-hand side shows a view perpendicular to the collison plane $(\phi=0)$, the right-hand side parallel to the collision plane $(\phi=\pi/2)$.

range $(\chi,\chi+\Delta\chi)$ together with the corresponding resolution of the velocity component $(\boldsymbol{u}_f)_y$. For a typical thermal energy $E=70$ meV elastic collision, the relative velocity is 1800 m/s. The final velocity u_f of the Ne$(3p)$ state is 340 m/s. This translates in a detuning range $2\Delta\omega_{\rm max}\approx 1.1(2\pi)$ GHz in case of the typical 593 nm probe-laser light. If a narrow-bandwidth dye laser is used, the natural linewidth $\Gamma\approx 10(2\pi)$ MHz determines the maximum obtainable resolution of approximately $0.01\Delta\omega_{\rm max}$ which corresponds to a velocity resolution $\Delta v_y\approx 7\ {\rm ms}^{-1}$. For high laser intensities power broadening may reduce this resolution. For the transitions we study in this paper, the probe parameters are listed in Table I.

Because the laser beam direction does not coincide with the relative velocity vector, the top angle χ does not correlate with a unique scattering angle θ, defined with respect to $\boldsymbol{v}_i$ (i.e., the z axis). These angles are depicted in Fig. 5. For top angles $\chi>0$ the resonant particles correspond to scattering angles $\theta_m<\theta<\pi-\theta_m$, with $\theta_m=\pi/2-\chi$. The differential cross section in the direction θ cannot be directly derived from the signals measured as a function of χ. Only for $\chi=0$ (probing the ''pole cap'') does the measured signal directly translate into $\theta=\pi/2$, albeit with a rather poor resolution. For other angles χ the following relation between scattering angle θ and χ holds:

$$\theta(\chi,\zeta)=\arccos(\sin\chi\,\cos\zeta), \tag{6}$$

TABLE I. Probe parameters for the $\alpha_7\rightarrow\alpha_7$ elastic and $\alpha_9\rightarrow\alpha_8$ inelastic transitions in the Ne$(3p)$ multiplet.

	$\alpha_7\rightarrow\alpha_7$	$\alpha_9\rightarrow\alpha_8$
ΔE (meV)	0	21
v_f (m/s)	2010	1680
u_i (m/s)	335	335
u_f (m/s)	335	280
$\lambda_{\rm prb}$ (nm)	593	583
$\Delta\omega_{\rm max}$ (2π MHz)	564	484

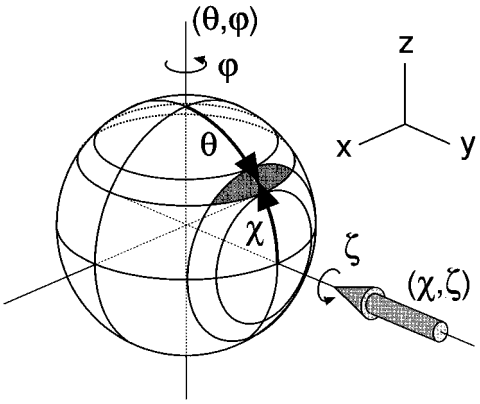

FIG. 5. Three-dimensional view of scattering sphere with the scattering cone between $(\theta, \theta+\Delta\theta)$ and the Doppler cone between $(\chi, \chi+\Delta\chi)$. The top angles (θ,ϕ) and (χ,ζ) are defined with respect to the z axis and the y axis, respectively.

where ζ denotes the azimuthal angle about the laser probe axis (y axis).

C. Pump-probe laser considerations

1. Pump laser

Two different laser systems are available for our experiment, (i) a dye laser using Rhodamine-DCM dyes and (ii) a diode laser with weak optical feedback.

The performance of these two systems is given in Table II. The pump laser excites either the $^3P_0$ or $^3P_2$ state of the Ne($3s$) configuration to one of the fine structure states of the Ne($3p$) multiplet. The pump laser is frequency stabilized by optimizing the absorption in a Ne discharge. For a dye laser, extra attention has to be paid to the alignment of the laser beam due to its narrow linewidth. This is extensively discussed in Ref. [19].

The transition wavelengths vary in the range $588\ \text{nm} < \lambda < 744\ \text{nm}$. For the initial states we will concentrate on the wavelengths listed in Table III. These fine structure states can be excited with a dye laser operating on Rhodamine 6G or DCM. Two different diode laser systems are available for Ne excitation: $\lambda_{\text{pmp}} = 653$ nm for $(^3P_0 \rightarrow \alpha_7)$ and $\lambda_{\text{pmp}} = 633$ nm for $(^3P_2 \rightarrow \alpha_8)$. For the transitions in this paper we use a diode laser for preparing α_7 states and we use a dye laser for exciting the Ne($3s, ^3P_2$) states to one of the α_4, α_8, or α_9 states.

2. Probe laser

To select a probe transition we must meet the following demands: (i) the wavelength λ_{prb} must be attainable by our lasers, (ii) we have to be able to single out the LIF wavelength λ_d (Fig. 1) with narrow-band interference filters in order to suppress competing fluorescence signals produced in the Ne-source or in the collision process, (iii) the lifetime of the upper state $|d\rangle$ must be comparable to that of the $|p\rangle$ state to guarantee sufficient fluorescence signal when saturating the $|p\rangle \rightarrow |d\rangle$ transition, and finally (iv) the branching ratio must be large for the studied decay transition (λ_d) to produce sufficient signal.

TABLE III. Wavelengths in nm for the pump transitions of the metastable Ne($3s$) states to a Ne($3p, \alpha_k$) state.

Ne($3s$)	Ne($3p,\alpha_4$)	Ne($3p,\alpha_7$)	Ne($3p,\alpha_8$)	Ne($3p,\alpha_9$)
$^3P_0$		653.288		
$^3P_2$	594.483	621.728	633.443	640.225

Based on these criteria we have selected the Ne($3p$)→Ne($4d$) transition for probing the final Ne($3p$) states. Due to the large energy gap between the α_9 and α_{10} states the decay lines of the Ne($4d$)→α_{10} transition are located around 534 nm and can be separated out easily from the other decay lines. This makes them suitable for detection without being disturbed by laser light or decay lines from the Ne($3p$) multiplet. In this paper we limit ourselves to the probing of the final states Ne($3p,\alpha_7$) and Ne($3p,\alpha_8$). The transition lines from the α_7 and α_8 states to the Ne($4d$) multiplet are listed in Table IV, together with their branching ratios A_{ki}/A_k. The large branching ratios of the subsequent transitions to the α_{10} state make them suitable for the LIF technique. All the probe line wavelengths are easily attainable with a dye laser. The linewidth of the probe transition is approximately $20(2\pi)$ MHz, determined by the lifetime of both the $|p\rangle$ and $|d\rangle$ states.

III. EXPERIMENTAL SETUP

A. Crossed beam apparatus

To analyze the final states of intramultiplet mixing collision processes we use the experimental setup used previously for total cross section measurements. In this paper we briefly review the apparatus, for details the reader is referred to Refs. [19, 20]. In Fig. 6 a schematic view of the crossed beam apparatus is given. The scattering center is formed by the intersection of the Ne beam, the He beam, and the pump-laser beam. The metastable Ne($3s$) atoms are produced in a thermal discharge source [25]. The He beam is obtained through a skimmerless supersonic expansion. Fluorescence of the initial and final Ne($3p$) states is efficiently collected

TABLE II. Performance of the ring dye-laser system compared to the diode-laser system.

System	Dye laser	Diode laser
λ range	550–660 nm	≈630, ≈650, ≈670, 750–850 nm
Linewidth	<10 MHz	20–100 MHz[a]
Power	>200 mW	<10 mW
Frequency drift	<10 MHz/min[b]	<100 MHz/min[c]

[a]No strong optical feedback.
[b]Locked to internal frequency reference.
[c]Not locked to external frequency reference.

TABLE IV. Wavelengths for the probe transitions of Ne$(3p,\alpha_f)$ to the Ne$(4d)$ $(K)_J$ states in the notation of jl coupling. The corresponding branching ratios A_{ki}/A_k are indicated as well.

$4l_v(K)_j$ Ne$(4d)$	Ne$(3p,\alpha_7)$		Ne$(3p,\alpha_8)$		Ne$(3p,\alpha_{10})$	
	λ (nm)	A_{ki}/A_k (%)	λ (nm)	A_{ki}/A_k	(%) λ (nm)	A_{ki}/A_k (%)
$4d(3/2)_2$	591.903	3.3	581.662	1.7	533.078	44.3
$4d(1/2)_1$	593.175	0.0	582.891	2.6	534.109	63.7
$4d(1/2)_0$	593.446	9.3			534.328	74.4

by a parabolic mirror and focused onto a photomultiplier. Wavelength selection is realized using narrow-band interference filters. Absolute values of the cross sections can be determined because the relative detection efficiencies for the initial- and final-state fluorescence are known. Due to the small dimensions of this atypical crossed beam apparatus with its efficient photon collection we can achieve typical count rates of 10^3 (counts/s)/Å^2 for the two-vector correlation experiment of the intramultiplet mixing processes of Eq. (1). Typical performance conditions of the apparatus are given in Table V.

The velocity distribution of Ne atoms produced by the thermal discharge source is determined through time-of-flight (TOF) measurements. In the compact crossed beam setup we use a laser chopper. With a flight path of only 100 mm the TOF experiment requires small time channels ($\tau=20$ μs). The result of a typical measurement is given in Fig. 7. From the analysis of these data we find an average velocity $\langle v_{\rm Ne}\rangle=960\pm30$ m/s and a characteristic velocity spread $\alpha=380$ m/s. Combined with the He beam velocity distribution we find for the average relative velocity $\langle v_i\rangle\approx1800$ m/s and the corresponding average collision energy is estimated at $\langle E\rangle=70$ meV.

The Ne$(3s)$ beam, traveling in the x direction, is attenuated by elastic scattering with He atoms. The probability for elastic scattering in travel distance $(x,x+dx)$ is given by the product $n_2(\boldsymbol{r})dxQ^{\rm el}$, with $n_{\rm He}$ the local He beam density and $Q^{\rm el}$ the effective total cross section for elastic scattering. The total transmission probability for reaching the scattering center is expressed in a factor T_i which is defined by

$$T_i=\int_{-\infty}^{0}\frac{v_i(x)}{v_{\rm Ne}}n_{\rm He}(x)Q^{\rm el}dx. \tag{7}$$

To obtain optimal collision-induced fluorescence [26] this transition probability is taken close to $T_i\approx1/e$ by regulating the He beam density $n_{\rm He}$. The interaction length of the Ne$(3s)$ states with the He beam upstream of the pump-laser beam is denoted by l_s, which is typically $l_s\approx2$ mm in our apparatus. The flux of unscattered metastable Ne$(3s)$ atoms arriving at the scattering center is denoted by $\dot{N}_s$. The value of this quantity can be estimated using Table V. The flux of Ne$(3s)$ states is given by $\dot{N}_s=I_{\rm Ne(3s)}\Omega_{\rm scat}T_i$, from which we find $\dot{N}_s\approx1.1\times10^9$ s^{-1}.

The Ne$(3s)$ states are excited to the initial Ne$(3p)$ state with an efficiency $f_{\rm pmp}$. Taking into account the natural abundance of the ^{20}Ne isotope (90%) together with the statistical distribution over the magnetic sublevels results in ef-

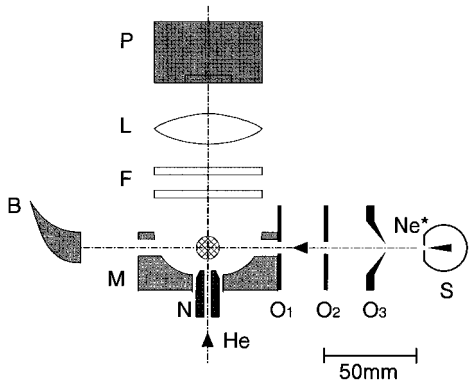

FIG. 6. Schematic view of the crossed beam apparatus. (S) Ne$(3s)$ metastable atom source; (O_1) beam-defining aperture (diameter equal to 1 mm); (O_2) extra aperture (diameter equal to 1 mm); (O_3) skimmer (diameter equal to 0.5 mm); (M) parabolic mirror; (B) beam dump; (N) nozzle; (F) interference filters; (L) collimating lens; (P) photomultiplier.

TABLE V. Typical performance conditions of the experimental setup.

Name	Quantity	Typical value	Units
Atomic beams			
Ne$(3s)$ beam intensity	$I_{\rm Ne(3s)}$	9×10^{12}	s^{-1} sr^{-1}
Source-scattering center distance	L	100	mm
Solid angle acceptance of Ne beam	$\Omega_{\rm scat}$	4×10^{-4}	sr
Ne flow velocity	$v_{\rm Ne}$	960	m/s
Speed ratio	$S=v/\alpha$	2.5	
He velocity	$v_{\rm He}$	1800	m/s
He density	nHe	1×10^{20}	m^{-3}
Transmission factor	T_i	$1/e$	
Initial relative velocity	v_i	2000	m/s
Average collision energy	E	70	meV
detection for Ne$(4d)$ line			
Photomultiplier Quantum efficiency	$\eta_{\rm qe}$	0.15	
Collection efficiency of optical system	$\eta_{\rm os}$	0.40	
Filter transmission	$T_{\rm filt}$	0.6	
Branching ratio	A_{ki}/A_k	0.6	

ficiencies $f_{\mathrm{pmp}}=0.15$ and $f_{\mathrm{pmp}}=0.75$ for the $^3P_0$ and $^3P_2$ states, respectively. Hence the flux of initial Ne($3p$) states is given by

$$\dot{N}_p = f_{\mathrm{pmp}} \dot{N}_s . \tag{8}$$

Because of the short lifetime $\tau=20$ ns of the Ne($3p$) states, the life path is only $l_p=20$ μm, which results in a much smaller collision probability than for the Ne($3s$) states.

The maximum resolution $\Delta\omega/\Delta\omega_{\max}\approx 0.01$ in the final velocity component decreases the performance of 10^3 (counts/s)/Å^2 for the total cross section for intramultiplet mixing to approximately 10 (counts/s)/Å^2 for the velocity-resolved differential cross section. Therefore an adequate suppression of background signal caused by scattered laser photons and photons produced in the Ne($3s$) source is necessary. Because of the large separation of the selected fluorescence line ($\lambda_d\approx 530$ nm) from other decay lines we planned to use a 10 nm broad transmission filter (see Table IV). The detection efficiency for collecting light from this decay line is given by $\eta_{\mathrm{det}}=\eta_{\mathrm{qe}}\eta_{\mathrm{os}}T_{\mathrm{filt}}A_{ki}/A_k$ and can be determined using Table V resulting in $\eta_{\mathrm{det}}=2\times 10^{-2}$.

The Ne($3s$) source causes a huge background signal of 180×10^3 (counts/s) in combination with the 10 nm transmission filter, thus far exceeding the expected differential fluorescence signal. Using a beam-defining aperture in front of the parabolic mirror (O_1 in Fig. 6) this background was reduced to 10^3 counts/s. Apparently, light emitted from the source enters the detection system through reflections in the apparatus. This background is further reduced to 200 counts/s by painting parts in the detection chamber black and by installing an extra aperture with 1 mm diameter between the skimmer and the downstream aperture in front of the parabolic mirror (O_2 in Fig. 6). Because light is also being emitted in the Ne expansion downstream of the skimmer, this extra aperture prevents these photons from reflecting in the parabolic mirror. The remaining background is further reduced to 50 counts/s using a 1 nm bandwidth transmission filter.

B. Pump laser

A temperature- and current-stabilized diode laser is used for populating the initial α_7 state. Weak optical feedback is used to enlarge the lasing range such that the desired wavelength can be reached [27]. The laser is frequency stabilized by maximizing the laser beam absorption in a Ne rf discharge using electronic feedback on the laser diode current. The linewidth of the diode laser is measured in a frequency scan where we monitor fluorescence of the Ne($3p$) state. Taking into account the geometrical beam divergence and the natural linewidth $\Gamma=8(2\pi)$ MHz we find an effective linewidth of $\gamma_{\mathrm{eff}}=50(2\pi)$ MHz, reflecting the broad linewidth of the laser diode. The experimental setup of the diode laser is shown in Fig. 8(a).

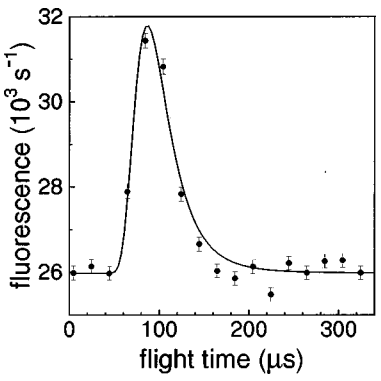

FIG. 7. Typical time-of-flight measurement for Ne($3s$) atoms performed with a flight path $L=100$ mm. From this we derive a flow velocity $\langle v\rangle=956$ m/s and a characteristic velocity spread $\alpha=384$ m/s for the velocity distribution.

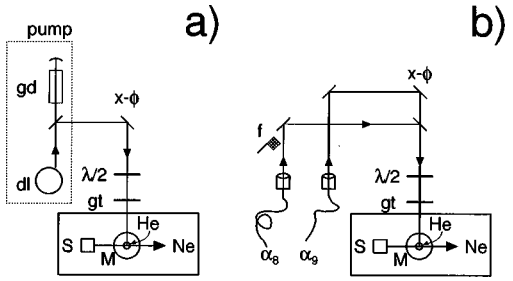

FIG. 8. Schematic view of the pump-laser setup. For elastic and inelastic collisions we use setup (a) or setup (b), respectively. (s) Ne metastable source; (dl) diode laser; (gd) gas discharge; (x-ϕ) computer adjustable mirror; ($\lambda/2$) half-lambda plate (gt) Glan-Taylor polarizing prism; (α_8) dye laser tuned at $^3P_0\rightarrow\alpha_8$ transition; (α_9) dye laser tuned at $^3P_0\rightarrow\alpha_9$ transition.

For populating one of the initial α_4, α_8, or α_9 states we use a cw dye laser which is stabilized on the absorption in a Ne discharge cell. The laser beam is transported through a single mode optical fiber to preserve the linear polarization. This is shown in Fig. 8(b). The polarization of the pump laser is rotated by a $\lambda/2$ plate. Nonlinear components are eliminated by a Glan-Taylor prism.

When we study the inelastic transition $\alpha_9\rightarrow\alpha_8$, an auxiliary laser beam is used for populating the final α_8 state directly by exciting the $^3P_2$ states. This facilitates the stabilization of the probe-laser frequency to the desired transition line, which will be discussed in Sec. VI. This additional laser beam is blocked during the actual collision experiment.

C. Probe laser

The probe-laser setup is schematically shown in Fig. 9. We use a standing wave cw dye laser locked to the transmis-

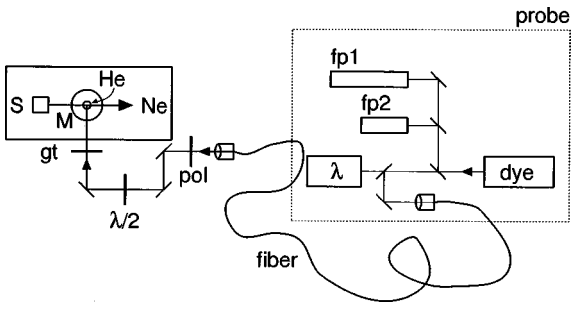

FIG. 9. Schematic view of the probe-laser setup. (dye) standing wave dye laser; (fp1) monitoring étalon with 150 MHz FSR; (fp2) temperature-stabilized locking étalon; (λ) wavelength meter; ($\lambda/2$) half-lambda plate (gt) Glan-Taylor polarizing prism; (pol) polarizer.

sion profile of a temperature-stabilized Fabry-Pérot étalon. By piezoelectric regulation of this étalon, the dye-laser frequency can be tuned over a range of $3(2\pi)$ GHz. Recording the fringes on a $150(2\pi)$ MHz monitoring étalon provides a calibration of the frequency scale. The drift of the laser frequency is less than $1(2\pi)$ MHz per minute, which is small in comparison with the probe transition linewidth of $10(2\pi)$ MHz. For accurate alignment, the laser beam is transported through a single mode optical fiber from the dye laser to the apparatus.

Absorption of the probe-laser beam in a Ne discharge is impractical to optimize the laser frequency of the probe laser due to the small Ne($3p$) population in the discharge. Therefore we use the Ne($3p$) states produced in the scattering center for finding the probe wavelength. In the case of the inelastic collision experiment an auxiliary laser is used for populating the final Ne($3p$) state with subsequent optimization of the probe wavelength. We monitor the fluorescence from the Ne($4d$) state while making a scan of the probe-laser frequency reference. Once the probe transition line is found, the laser frequency is locked to the temperature-stabilized étalon with a small drift (<5 MHz/min). Using a piezoelectric detuning of this cavity, we can fix the laser detuning to its desired value $\delta_{\rm prb}$. During a measurement the probe wavelength is optimized periodically (every 10 min) to compensate for the frequency drift of the probe laser.

The probe-laser power in the collision experiment is approximately 3 mW, which is sufficient to saturate the probe transition. The waist position and size of the probe laser are chosen such that a good overlap with the pump laser is achieved. The waist size of the probe laser is typically 2 mm, whereas the waist size of the pump laser is only 1 mm. The polarization of the probe laser is rotated with a $\lambda/2$ plate and subsequently cleaned up by a Glan-Taylor prism.

IV. DOPPLER PROBING OF Ne($3s,^3P_0,^3P_2$) ELASTIC SCATTERING

Applying the Doppler probing technique to the final $|p\rangle$ states is not trivial due to the small final-state populations produced in our collision experiment. A suitable system for testing the Doppler probing technique is elastic scattering of $|s\rangle$ states which are scattered over their full interaction length with the supersonic He expansion. From the transmission probability $T_i \approx 1/e$ in Eq. (7) it follows that approximately 70% of the $|s\rangle$ particles are scattered by the He atoms before reaching the scattering center. The $|s\rangle$ states are excited to $|p\rangle$ states using a tunable pump laser. The decay fluorescence of the $|p\rangle$ states is measured as a function of the detuning $\delta_{\rm pmp}$ of the pump laser. The relation between the detuning $\delta_{\rm pmp}$ and the top angle χ of the ''Doppler'' cone is analogous to Eq. (5).

We use the tunable dye laser (used as probe laser in a pump-probe experiment) to excite the $^3P_2 \rightarrow \alpha_4$ transition. The effective linewidth $\gamma_{\rm eff}$ is mainly determined by the natural linewidth Γ and only to a small extent by the laser linewidth $\gamma_{\rm pmp}$ and the geometrical divergence of the Ne($3s$) beam. We measure the decay fluorescence of the α_4 state as a function of the detuning $\delta_{\rm prb}$ with the He beam switched on and off, respectively. The result of such a scan is plotted in Fig. 10. With the He beam on, we have an effective transmission (or beam attenuation) of $T_i \approx 30\%$. For comparison, we show the signal with the He beam switched off multiplied by the same attenuation factor T_i. For a detuning $\delta_{\rm prb} \geqslant 20(2\pi)$ MHz the small angle scattering of the Ne($3s$) states contributes significantly to the observed signal.

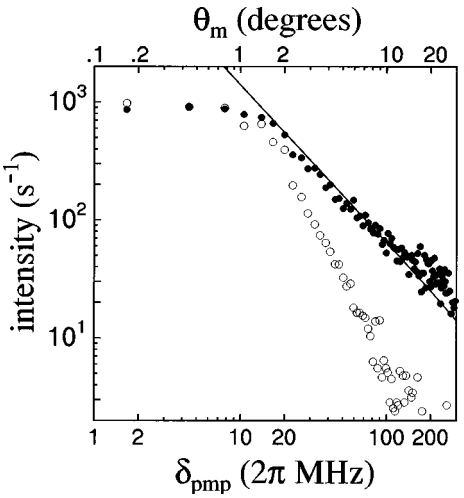

FIG. 10. Direct fluorescence for the elastic scattering of Ne($3p,^3P_2$) states as a function of the detuning $\delta_{\rm prb}$ with the He beam switched on (filled markers) and off (open markers). The fluorescence for the He beam switched off is scaled with the attenuation factor $T_i = 1/e$. The solid line represents the model function of Eq. (11) for classical small angle scattering.

The small angle scattering of $|s\rangle$ states is in good approximation determined by the long-range part of the attractive potential [28,29], which is given by

$$V(r) = -C_6/R^6, \tag{9}$$

with R being the internuclear distance. For scattering angles $\theta < \theta_0$, with $\theta_0 = (4\pi/k^2 Q)^{1/2}$ a quantum-mechanical scaling angle, diffraction phenomena dominate the differential cross section. In our case where $\theta_0 \approx 4$ mrad, this region is not relevant. For $\theta > \theta_0$ small angle scattering is fully described by classical mechanics, i.e., the equivalent of refraction. For a C_6 potential the differential cross section is related to the scattering angle as [28]

$$\sigma(\theta)/\sigma(0) = 0.285(\theta/\theta_0)^{-7/3} \quad (\theta > \theta_0), \tag{10}$$

where $\sigma(0)$ denotes the forward scattering cross section.

The measured signal is proportional to the integral of this differential cross section over the Doppler cone with top angle χ, as indicated in Fig. 5. Using Eqs. (5) and (10) we derive in Appendix A an expression for the detected signal

$$S(\delta_{\rm pmp}) = C(\gamma_{\rm eff}, n_{\rm He}, l_p)\left[\frac{\pi}{2} - \chi(\delta_{\rm pmp})\right]^{-4/3}, \tag{11}$$

where the scaling constant C contains several experimental parameters. Note that this approximation is only valid for $(\pi/2 - \chi) < 0.5$ (rad) where it is accurate within 1%. The top angle χ is written as

$$\chi(\delta_{\rm pmp}) = \arccos\left(\frac{\delta_{\rm pmp}}{\Delta\omega_{\max}}\right), \quad |\delta_{\rm pmp}| < \Delta\omega_{\max} \tag{12}$$

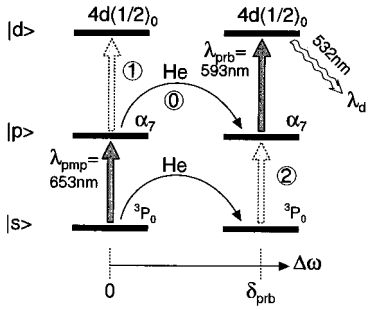

FIG. 11. Pump-probe scheme for the elastic $\alpha_7 \rightarrow \alpha_7$ transition. The dashed arrows 1 and 2 indicate competing excitation processes which contribute to the signal.

where we used Eq. (5). In Fig. 10 the experimental data are plotted on a log-log scale together with the model function of Eq. (11). For a detuning corresponding with angles θ_m in the range $0.03 < \theta_m(\text{rad}) < 0.5$ there is very good agreement with the relation of Eq. (11). A background of approximately 30 Hz is subtracted. Obviously, the Doppler technique probes the $\theta^{-7/3}$ character of the differential cross section. We conclude that the Doppler technique works very well and can be utilized in our proposed pump-probe experiment.

V. Ne($3p,\alpha_7$) ELASTIC SCATTERING

A. Measuring scheme

The excitation and detection scheme for $\alpha_7 \rightarrow \alpha_7$ elastic scattering is shown in Fig. 11. We use a $\lambda_{\text{pmp}} = 653$ nm diode laser to excite the $^3P_0$ states and a dye laser at $\lambda_{\text{prb}} = 593$ nm probes the α_7 through excitation to a $J_d = 0$ state of the Ne($4d$) multiplet. This $J_s = 0 \rightarrow J_p = 1 \rightarrow J_d = 0$ scheme facilitates the analysis. The decay line of the Ne($4d$) state to the Ne($3p,\alpha_{10}$) state at $\lambda_d = 534$ nm is detected with an interference filter at 534 nm with a 1 nm bandwidth.

In Fig. 11 three contributions to the detected 534 nm signals are indicated and numbered. The actual collision process that we want to investigate is denoted by the arrow 0. The dashed arrows 1 and 2 show the competing excitation processes representing the *direct* probing of unscattered α_7 states and the $^3P_0$ states that are scattered before they are excited by the 653 nm pump laser. The suppression of the signal due to these competing processes requires a detailed analysis of these signals. In this analysis we will not take into account the $|M_J|$ dependency of the scattering process.

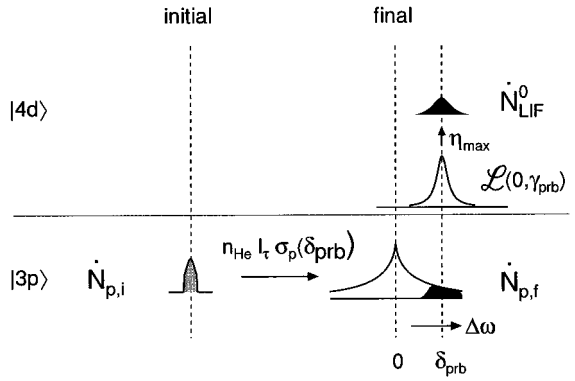

FIG. 12. Schematic representation of signals in the elastic scattering probing scheme. The symbols are declared in the text.

We start out by analyzing the desired process, i.e., the probing of elastic scattered $|p\rangle$ states. This process is schematically depicted in Fig. 12. In the scattering center we have flux $\dot{N}_{p,i}$ of $|p\rangle$ states given by Eq. (8). The collision rate $\dot{N}_{p,f}(\delta_{\text{prb}})$ is determined by the effective density-length product

$$\dot{N}_{p,f}(\delta_{\text{prb}}) = n l_\tau \sigma_p(\delta_{\text{prb}}) \dot{N}_{p,i}, \tag{13}$$

where $l_\tau = v_i \tau$ denotes the ''life path'' of the short-lived state and $\sigma_p(\delta_{\text{prb}})$ is the differential cross section for scattering into the Doppler cone about the probe-laser beam with top angle $\chi(\delta_{\text{prb}})$, as defined in Eq. (5). These final states are resonant with the probe laser. Therefore they will contribute to the desired LIF fluorescence $\dot{N}^0_{\text{LIF}}$ with the maximum efficiency η_{max}, which depends on the lifetimes of the $|p\rangle$ and $|d\rangle$ states,

$$\dot{N}^0_{\text{LIF}}(\delta_{\text{prb}}) = \eta_{\text{max}} \dot{N}_{p,f}(\delta_{\text{prb}}). \tag{14}$$

The total LIF signal including the two competing processes is given by

$$\dot{N}_{\text{LIF}} = \dot{N}^0_{\text{LIF}} + \underbrace{\dot{N}^1_{\text{LIF}} + \dot{N}^2_{\text{LIF}}}_{\text{undesired}}.$$

The two competing processes depend on the laser polarization configuration because no scattering occurs during the time interval between the pump and the probe processes. When using perpendicular laser polarizations for the $J_s = 0 \rightarrow J_p = 1 \rightarrow J_d = 0$ pump-probe scheme or parallel polarizations in the case of $J_s = 0 \rightarrow J_p = 1 \rightarrow J_d = 1$ excitation these processes can be suppressed considerably. This suppression is described by a factor η_{pol} which can range typically from 1 (no suppression) to 10^{-3} (maximum suppression). The undesired contributions are estimated in Appendix B in terms of experimental parameters.

Two handles are available to suppress the competing processes: (i) the polarization configuration in combination with the $|s\rangle$-$|p\rangle$-$|d\rangle$ pump-probe scheme which determines η_{pol}, and (ii) the detuning δ_{prb} of the probe laser. The ratios $\dot{N}^1_{\text{LIF}}/\dot{N}^0_{\text{LIF}}$ and $\dot{N}^2_{\text{LIF}}/\dot{N}^0_{\text{LIF}}$ determine whether it is possible to study the elastic scattering process of Eq. (1). The first ratio can be estimated as

$$\frac{\dot{N}^1_{\text{LIF}}}{\dot{N}^0_{\text{LIF}}} \simeq 10^4\, \eta_{\text{pol}} \left(\frac{\gamma}{2\,\delta_{\text{prb}}} \right)^2, \tag{16}$$

where γ is the linewidth of the $|p\rangle$-$|d\rangle$ transition, determined by the lifetimes of both states. The second ratio can be approximated by

$$\frac{\dot{N}^2_{\text{LIF}}}{\dot{N}^0_{\text{LIF}}} \simeq 100\, \eta_{\text{pol}}. \tag{17}$$

Thus we conclude that it is essential to efficiently suppress the direct excitation processes ($\eta_{\text{pol}} \approx 10^{-3}$) in order to study the elastic process.

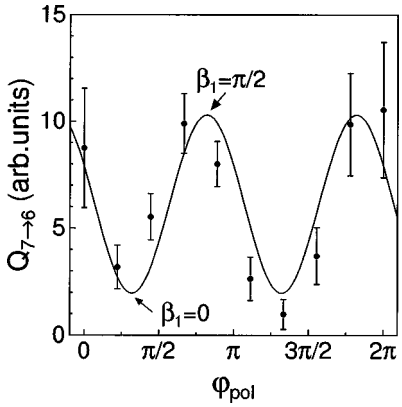

FIG. 13. Typical measurement of the polarized-atom cross section $Q_{7\to6}$, as a function of the polarization angle $\varphi_{\rm pol}$ of the pump laser. The corresponding angle β with respect to the initial relative velocity is indicated.

B. Results

It is important to know the orientation of the relative velocity vector $\boldsymbol{v}_i$ with respect to the laboratory frame indicated by angle φ_0 in Fig. 4. We calibrate the laser polarization angle $\varphi_{\rm pol}$ defined with respect to He velocity by performing a two-vector correlation experiment giving the offset angle φ_0. The result of this measurement is shown in Fig. 13 where β_1 denotes the angle between the laser polarization $\boldsymbol{E}_{\rm pmp}$ and the relative velocity $\boldsymbol{v}_i$. Theoretically, a $\cos(2\beta_1)$ behavior is expected with a minimum for $\beta_1=0$ and a maximum for $\beta_1=\pi/2$. In a least-squares analysis we determine the relation between the two angles as $\beta=\varphi_{\rm pol}-\varphi_0$, yielding an offset $\varphi_0=32°$. The offset φ_0 also follows from the average velocities $v_{\rm Ne}\approx1000$ m/s and $v_{\rm He}\approx1800$ m/s of the crossed beams, which yields $\varphi_0=\arctan(v_{\rm Ne}/v_{\rm He})\approx29°$.

We measured the LIF signal as a function of the detuning $\delta_{\rm prb}$ of the probe laser for a parallel laser configuration ($\eta_{\rm pol}=1$). The probe parameters are given in Table I. In Fig. 14 the results are shown for the He beam switched on and off. We adjusted He beam density $n_{\rm He}$ such that the transmission factor is equal to $T_i\approx1/e$. The LIF signal in Fig. 14 for the He beam switched off is scaled with T_i.

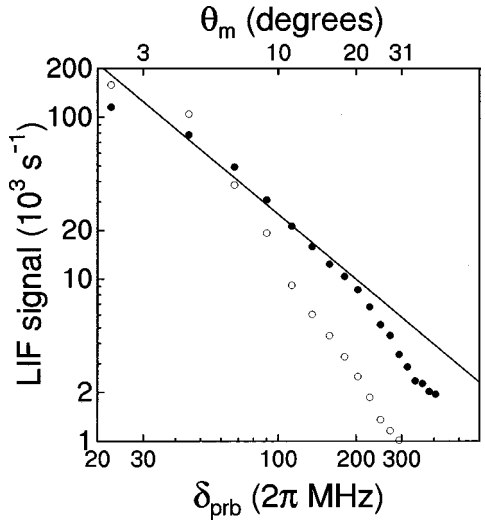

FIG. 14. LIF signal ($\eta_{\rm pol}=1$) for the elastic scattering of Ne$(3p,\alpha_7)$ states as a function of the detuning $\delta_{\rm prb}$ with the He beam switched on (filled markers) and off (open markers). The fluorescence for the He beam switched off is scaled with the attenuation factor $T_i=1/e$. The solid line represents the $\delta_{\rm prb}$ dependence of the model function of Eq. (11) for classical small angle scattering.

According to the preceding section, the contribution from the competing processes $\dot{N}^1_{\rm LIF}$ and $\dot{N}^2_{\rm LIF}$ are not suppressed when $\eta_{\rm pol}=1$. Therefore the LIF signal will be dominated by the elastic scattering of Ne$(3s)$, i.e., $\dot{N}^2_{\rm LIF}$, which causes the broadening that can be seen in Fig. 14. We analyze the LIF-signal measurement with the classical small angle scattering expression of Eq. (11). For a detuning $\delta_{\rm prb}<200(2\pi)$ MHz which corresponds to scattering angles $\theta_m<20°$ we see a fair agreement.

For the $J_s=0\to J_p=1\to J_d=0$ pump-probe scheme the *direct* excitation ($\eta_{\rm pol}=1$ for parallel laser configuration) with the probe laser on resonance and the He beam switched off results in a huge LIF signal of 300×10^3 counts/s. This is efficiently reduced in the perpendicular laser configuration to only 300 counts/s from which follows $\eta_{\rm pol}\approx10^{-3}$. This count rate is superimposed on the background signal (source plus pump laser plus probe laser) of 260 counts/s. The 300-count/s ''leakage'' reduces with increasing detuning $\delta_{\rm prb}$. For $\delta_{\rm prb}=400(2\pi)$-MHz detuning the leakage signal is smaller than the noise on the background signal. In such a far off-resonance measurement we observe no significant difference between the LIF signal measured with the He beam switched on or off. In the case of perpendicular laser polarizations the expected LIF signal resulting from M_J-changing collisions is estimated in the range 5–10 counts/s. The statistical noise can be reduced by increasing the measuring time. However, at the same time the drift in source operation and laser light power induces a fluctuation in the LIF signal of the same order of magnitude as the desired signal.

We conclude that the signals for M_J-changing collisions are too small in comparison to the drift in the background signal. Quantum simulations show that the M_J-preserving collisions have cross sections about a factor 10 higher. However, the competing processes which contribute to the LIF signal cannot be reduced in this configuration since $\eta_{\rm pol}=1$.

VI. Ne$(3p,\alpha_9\to\alpha_8)$ INELASTIC SCATTERING

A. Measuring scheme

The pump-probe scheme for the inelastic collision $\alpha_9\to\alpha_8$ is shown in Fig. 15. In this scheme the two competing contributions originating from the direct excitation of initial $|p\rangle$ states and from excitation of scattered metastable $|s\rangle$ states are eliminated. In contrast with the elastic scattering process, it is clear that now all laser configurations, i.e., parallel, perpendicular, and circular polarizations, can be studied.

By pumping from the $^3P_2$ state, a factor 5 is gained in $|p\rangle$-state population in comparison with the excitation from the $^3P_0$ states. Note, however, that we are not dealing with a single magnetic sublevel anymore. The two-level character of the pump transition $^3P_2\to\alpha_9$ allows the $^3P_2$ states to be excited typically 25 times because the atoms reside in the laser beam about $\Delta t\approx1$ μs$=50\tau$. Although the cross sections for the inelastic transitions are generally much smaller

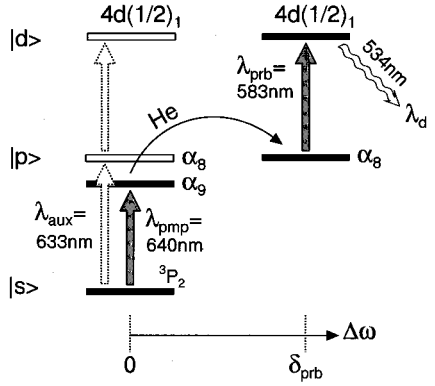

FIG. 15. Pump-probe scheme for inelastic $\alpha_9 \rightarrow \alpha_8$ scattering. The dashed arrow indicates an auxiliary laser to populate the α_8 states for tuning the probe laser to the resonance frequency, i.e., finding the ''zero'' point for the probe laser.

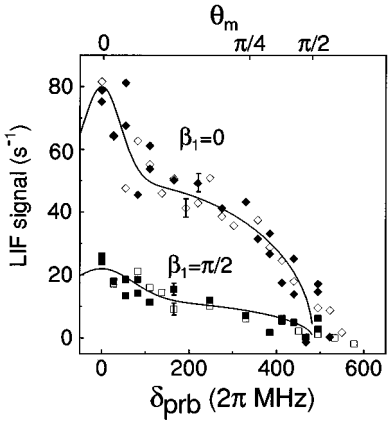

FIG. 16. LIF signal measured as a function of the detuning δ_{prb} for the $\alpha_9 \rightarrow \alpha_8$ transition for different combinations (β_1, β_2) of linear polarizations: diamonds $(\beta_1 = 0)$; squares $(\beta_1 = \pi/2)$; open markers $(\beta_2 = 0)$; filled markers $(\beta_2 = \pi/2)$. Two typical error bars are indicated. The solid lines represent model functions for an empirical description of the data.

than their elastic counterparts, the collision signals are enlarged by the much longer interaction length $25 l_\tau \approx 0.5$ mm in this special configuration.

This inelastic scattering process introduces the problem of finding the probe-laser transition. In contrast with the elastic probing scheme the collision-induced α_8 states have to be used to find the probe transition line. Due to the small signals, the probe line cannot be detected during a coarse frequency scan. Therefore an auxiliary laser is used which is tuned to the $^3P_2 \rightarrow \alpha_8$ transition. Now the α_8 states can be populated sufficiently while scanning the probe laser.

B. Results

In our experiment typical background signals are 50 counts/s from light emitted from the source, 150 counts/s from the pump laser, and 250 counts/s from the probe laser, adding up to a total background signal of 450 counts/s. When the He beam is switched on an additional background signal of 10 counts/s is detected. This is caused by the altered conditions of the light production in the Ne expansion. These background signals are quite constant during a measurement and are determined every half hour. To obtain a good signal-to-noise ratio we measure 2000 s for each detuning of the probe-laser frequency. In between two measurements the frequency drift of the probe laser is compensated for by means of the auxiliary laser.

We measured the LIF fluorescence of the $|d\rangle$ state as a function of the probe-laser detuning δ_{prb}. The results for the four linear pump-probe polarization configurations, $(\beta_1, \beta_2) = (0,0)$, $(0,\pi/2)$, $(\pi/2,0)$, $(\pi/2,\pi/2)$, are shown in Fig. 16. We see a large dependency on the pump-laser polarization (β_1). An effect of the probe-laser polarization (β_2) cannot be observed. We use a model function for representing the data in a compact way. The only physical quantity which enters in this model function is the value of $\Delta\omega_{\max} = 486(2\pi)$ MHz (see Table I). We take the basis model function proportional to $[1-(\delta_{\mathrm{prb}}/\Delta\omega_{\max})^2]^{1/2}$. An additional Gaussian function describes the forward scattered peak around $\delta_{\mathrm{prb}} = 0$. We see perfect agreement of the cutoff at $\delta_{\mathrm{prb}} = \Delta\omega_{\max}$.

For the circular polarization we have performed measurements for the (σ^+, σ^+) and (σ^+, σ^-) configurations. The results are shown in Fig. 17. For the two polarization configurations we see a similar shape of the LIF signal. Comparing these results to the linear polarization measurements in Fig. 16 we see that the circular measurements have a concave shape whereas the linear data display a more convex shape. We use a Lorentzian shape function to represent the data of the form $[1+(\delta_{\mathrm{prb}}/\delta_0)^2]^{-1}$, with $\delta_0 = 250$ MHz. A cutoff at $\delta_{\mathrm{prb}} = \Delta\omega_{\max}$ is introduced by multiplying with a Heaviside function. For the (σ^+, σ^-) configuration this feature is pronounced in the experimental data.

Using the parameters of Sec. III A for the flux of Ne$(3s)$ in the scattering center $\dot{N}_{s,i} \approx 1.1 \times 10^9$ s^{-1} and the detection efficiency $\eta_{\mathrm{det}} = 2 \times 10^{-2}$ we can estimate the LIF signal for Doppler probing the $\alpha_9 \rightarrow \alpha_8$ transition. In Table VI typical quantities which determine the detected LIF signal are given. These quantities determine the collision probability $P_{\mathrm{col}} = n_{\mathrm{He}} l_{\mathrm{int}} Q_{9\rightarrow 8}$ and the probing efficiency $\eta_{\mathrm{LIF}} = \eta_{\max}\gamma_{\mathrm{prb}}/\Delta\omega_{\max}$. The expected LIF signal is written as the

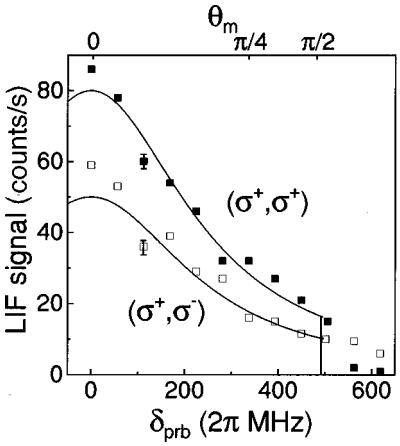

FIG. 17. LIF signal measured as a function of the laser detuning δ_{prb} for the $\alpha_9 \rightarrow \alpha_8$ transition for the circular polarization combinations (σ^+, σ^+) and (σ^+, σ^-) which are represented by the closed and open markers, respectively. The solid lines represent model functions for an empirical description of the data.

TABLE VI. Estimation of the expected signal for the $\alpha_9 \rightarrow \alpha_8$ pump-probe experiment.

	Units	Value	Total
n_{He}	m^{-3}	10^{20}	
$l_{int} \approx 25 l_\tau$	m	0.510^{-3}	$P_{col} = n_{He} l_{int} Q = 210^{-3}$
$Q_{9\rightarrow 8}$	$Å^2$	3.5	
η_{max}		0.1	$\eta_{LIF} = 10^{-3}$
$\frac{\lambda_{prb}}{\Delta\omega_{max}}$		0.01	

product $S = f_{pmp} \dot{N}_{s,i} P_{col} \eta_{det} \eta_{LIF} \approx 35$ counts/s. Note that this signal is an averaged value and that effects such as overlap of lasers, laser intensities, and the effect of the polarization configuration are not taken into account. Nevertheless, this estimate is in good agreement with the measured signal presented in Figs. 16 and 17.

The overlap of pump and probe laser in the scattering center is altered when changing the polarization configuration and hence the absolute value of the measured signals for the different polarization measurements cannot be compared directly. Therefore in the further analysis only the shape of the measured cross section data will be used.

VII. COMPARISON WITH THEORY

A. Coupled channels calculation

The intramultiplet mixing process of Eq. (1) is described quantum mechanically in a coupled channels calculation. Model potentials proposed by Hennecart and co-workers [22–24] serve as an input for this calculation. Manders *et al.* extended the model potentials with a repulsive branch [26] and performed calculations of polarized-atom cross sections with the coupled channels code. Good agreement was found between the calculated and experimental cross sections in the thermal collision energy range $E = 70–130$ meV. For superthermal collision energies in the range $E = 0.5–2$ eV the calculated values are higher than the experimental cross sections, as reported by Boom *et al.* [20]. Recently, this coupled channels program has been extended to incorporate an optical potential for describing the process of Penning ionization; it has been successfully applied to $Ne(3s/3p) + Ar$ collisions [30]. In that sense, the coupled channels calculations are a necessary tool for the description of these collision processes.

B. Numerical simulation

The basis of the simulation is formed by the scattering matrices calculated quantum mechanically in a coupled channels model. The pump-probe laser beam configuration enters the calculation in the form of two density matrices for initial-state preparation and final-state analysis, respectively. Next, an expression for the experimental Doppler cross section $\sigma(\chi)$ is derived. The simulation is described in detail in Ref. [31].

The simulation is set up for a general pump-probe configuration. In our case the pump laser is aligned along the y_{col} axis, perpendicular to the initial relative velocity $\boldsymbol{v}_i$. The collision frame $(x_{col}, y_{col}, z_{col})$ and the Doppler frame (x_d, y_d, z_d) are related by a rotation over the the Euler angles $(\phi, \psi, 0)$ as depicted in Fig. 18. The laser configuration used in our experiment with counterpropagating laser beams is described by the Euler angles $(\phi, \psi) = (\pi/2, -\pi/2)$. The angles (β_1, β_2) introduced in Sec. II A are now defined in terms of rotation angles around the z_{col} and z_d axis, respectively.

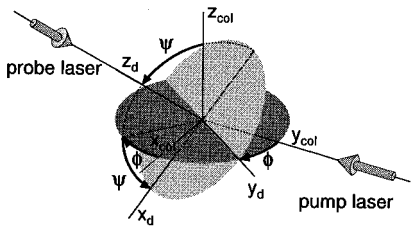

FIG. 18. The collision frame $(x_{col}, y_{col}, z_{col})$ and the Doppler frame (x_d, y_d, z_d) are related by a rotation over the the Euler angles $(\phi, \psi, 0)$. The preparation laser beam is aligned along the y_{col} axis, the pump-laser beam along the z_d axis.

Simulations have been performed for the differential Doppler cross section $\sigma(\delta_{prb})$ as a function of the polarization configuration of the pump-probe laser beams and the collision energy, with δ_{prb} the probe-laser detuning according to Eq. (5). Results of the simulation can be used either to investigate new pump-probe configurations or to compare to measured cross sections.

C. Elastic $\alpha_7 \rightarrow \alpha_7$ scattering

For the elastic process the quantum-mechanical results for the four linearly polarized laser configurations are shown in Fig. 19. A clear distinction between the parallel (0,0) and $(\pi/2, \pi/2)$ and the perpendicular $(0, \pi/2)$ and $(\pi/2, 0)$ laser polarization configuration can be seen. The parallel configuration probes the M_J-preserving collisions which are strongly forward peaked. The M_J-changing collision cross sections are more than a factor 10 smaller than the M_J-preserving collisions.

D. Inelastic $\alpha_9 \rightarrow \alpha_8$ scattering

Since the initial state α_9 with $J = 3$ is excited from the metastable $^3P_2$ state with $J = 2$, only the magnetic substates

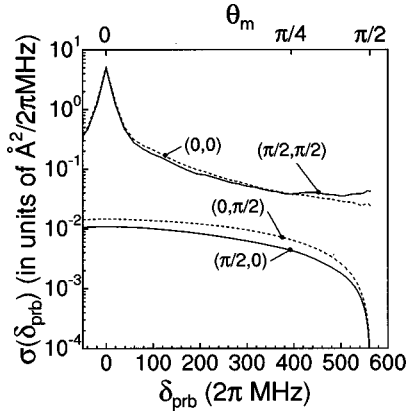

FIG. 19. Quantum-mechanical results for the $\alpha_7 \rightarrow \alpha_7$ transition at a collision energy $E = 70$ meV. The four basic linear polarization configurations with angles (β_1, β_2) are indicated.

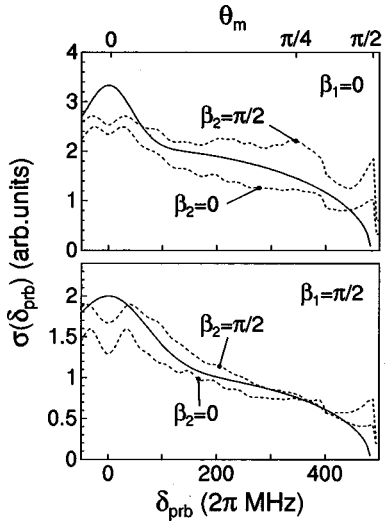

FIG. 20. Quantum-mechanical results for the $\alpha_9 \rightarrow \alpha_8$ transition averaged over the experimental energy distribution (dashed curves), compared with the (scaled) model functions representing the experimental results (solid curves) for linear polarization configurations with angles (β_1, β_2) as indicated.

in the range $M_J = -2,\ldots,2$ are symmetrically populated for linearly polarized light with a population distribution g_M. This weighted distribution (g_M) of incoherently populated magnetic substates is determined in a Monte Carlo simulation described in Ref. [32]. With this distribution we calculate the Doppler cross sections $\sigma(\delta_{\mathrm{prb}})$ for the four linearly polarized pump-probe configurations. For the two circular polarization configurations the distribution is given by $g_M = \delta_{3,M}$.

In our experiment the initial relative velocity has a broad distribution with an average value $\langle v_i \rangle = 2000$ m/s and a width of 300 m/s. In a coarse approximation we calculate the differential cross sections for three collision energies 55, 70, and 85 meV and use weight factors 0.6, 1.0, and 0.6 according to the energy distribution, respectively. The results of the simulation are shown in Figs. 20 and 21 for the linear and circular polarization configurations, respectively. We see a small difference in cross section values for different probe-laser polarizations.

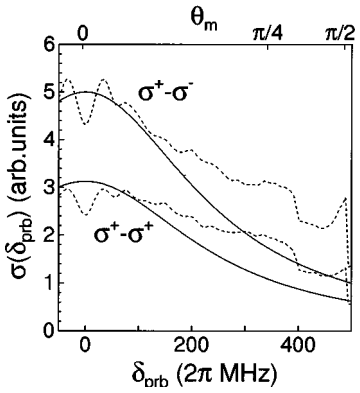

FIG. 21. Quantum-mechanical results for the $\alpha_9 \rightarrow \alpha_8$ transition averaged over the energy distribution (dashed curves), compared with the model functions (both scaled by the same factor) representing the experimental results (solid curves) for circular polarization configurations as indicated.

The simulated cross sections are compared with our measured data. We use different scaling factors for the $\beta_1 = 0$ and $\beta_1 = \pi/2$ measurements in the linear polarization configuration. When the polarization of the pump laser is rotated, its spatial position is slightly altered, leading to a different initial Ne$(3p)$ in the scattering center distribution and thus different scaling factors. Furthermore, due to the small nozzle-scattering center distance of 2 mm, both the collision energy and the He density vary rather strongly, over the scattering center. For instance, the He density changes by 10% for a change of 0.1 mm in this position. The large waist (2 mm) of the probe laser guarantees a good overlap with the scattering center and the results are insensitive for a rotation of the probe-laser polarization. In the case of the circular laser polarizations the two configurations (σ^+, σ^+) and (σ^+, σ^-) are obtained by changing the probe-laser polarization. A negligible effect is expected and a single scaling factor between simulated and experimental results is used.

E. Discussion

The quantum-mechanical simulations of the elastic scattering process suggest that the parallel configurations have larger cross sections than the perpendicular polarization configurations. Experimental signals for the parallel cross sections $(\eta_{\mathrm{pol}} = 1)$ are larger, but at the same time, there is a larger contribution of the undesired competing processes which scale with η_{pol}. Therefore only the perpendicular configurations, i.e., M_J-changing processes, are good candidates for future measurements with high intensity bright metastable beams.

It should be noted that in the numerical simulation the experimental convolution effects are neglected, except for a first order energy convolution as discussed above. Two other important effects should be mentioned. First, the geometrical divergence of the Ne$(3s)$ beam is characterized by a spread of 10 m/s in the direction of the probe laser beam which translates into an additional convolution with a block profile with a typical filter width of $30(2\pi)$ MHz. Second, the excitation process of the Ne$(3p)$ states does not occur at a single point in space. However, Monte Carlo simulations show that the position dependence of the collision energy, the detection efficiency, and the angle of the relative velocity cause an extra convolution which is not significant in comparison to the energy and perpendicular velocity spread [32].

VIII. PUMP-PROBE CONFIGURATION

In our experiment, the choice of counterpropagating pump- and probe-laser beams, both perpendicular to the initial relative velocity $\mathbf{v}_i$, is fully determined by the geometrical limitations of the setup. Access to the scattering center from other directions was not possible. This configuration results in an extra convolution of the differential cross section, which in general makes access to the physical information harder.

It is useful to investigate the advantages and disadvantages of this choice, as compared to the ideal situation of a pump-laser beam perpendicular to $\mathbf{v}_i$ and a probe-laser beam collinear with $\mathbf{v}_i$. The advantage of the latter choice is clear: a single detuning of the probe-laser beam corresponds to a

single polar angle θ with only an integration over the azimuthal angle ϕ. The choice for a pump-laser beam perpendicular to the initial relative velocity is also rather straightforward: by rotation of the polarization vector $\mathbf{E}_{\mathrm{pmp}}$ with respect to $\mathbf{v}_i$ we can easily prepare our aligned initial states. For a useful comparison of both configurations we plot the measured differential Doppler cross section in the ideal configuration as a function of the probe laser detuning ${}^{\mathrm{ideal}}\delta_{\mathrm{prb}}(\theta)$, with ${}^{\mathrm{ideal}}\delta_{\mathrm{prb}}=-\Delta\omega_{\max}$ corresponding to $\theta=0$ and thus $\delta_{\mathrm{prb}}=0$; the case ${}^{\mathrm{ideal}}\delta_{\mathrm{prb}}=0$ then corresponds to $\theta=\pi/2$ and thus $\delta_{\mathrm{prb}}=\Delta\omega_{\max}$. These data can be directly compared to the results in the experimental configuration in the range $0<\delta_{\mathrm{prb}}\leqslant\Delta\omega_{\max}$. In the ideal configuration, we do not consider the range $0<{}^{\mathrm{ideal}}\delta_{\mathrm{prb}}\leqslant\Delta\omega_{\max}$ (corresponding to scattering angles $\pi/2<\theta\leqslant\pi$), because there is no equivalent result in the experimental configuration. For simplicity, we limit our discussion to initial states with $J=1$ that are laser excited from the metastable $\mathrm{Ne}(3s,{}^3P_0)$ state using linear polarized light.

We first discuss the elastic $\alpha_7\rightarrow\alpha_7$ collisions, probed by a transition to a level with $J'=0$. For a parallel orientation of the pump and probe polarization vectors, i.e., $\mathbf{E}_{\mathrm{prb}}\|\mathbf{E}_{\mathrm{pmp}}\perp\mathbf{v}_i$, the measured Doppler differential cross section as a function of the laser detuning is quite similar for both the experimental and the ideal configuration. This can be easily understood. Due to the strongly peaked character of small angle scattering, the contribution at an angle χ in the experimental configuration is dominated by the region corresponding to the smallest angle $\theta=\pi-\chi$.

For a perpendicular orientation of the laser polarization vectors, i.e., $\mathbf{E}_{\mathrm{prb}}\perp\mathbf{E}_{\mathrm{pmp}}\perp\mathbf{v}_i$, we observe larger differences. First, the absolute value of the measured small angle Doppler cross sections is much smaller than for the parallel orientation. In this case, only $|\Delta M|$-changing collisions contribute at small angles, resulting in both the experimental and the ideal configuration in much smaller absolute values of the measured Doppler cross sections as compared to the parallel configuration. Second, the differential Doppler cross section in the experimental configuration has lost all of its oscillatory structure. At small angles, its magnitude is also a factor 5 less than the signal for the ideal configuration. Only at large angles $\pi/6<\theta\leqslant\pi/2$ do the two configurations show similar results.

Next, we investigate the inelastic $\alpha_5(J=1)\rightarrow\alpha_7(J=1)$ transition, probed by a transition to an upper level with $J'=0$. The reason for using this transition as a test case is the detailed understanding of its nature within a semiclassical model in terms of an avoided crossing [26]. In Fig. 22 we show the calculated results for the Doppler differential cross section for both configurations, plotted as a function of the corresponding detuning δ_{prb} or ${}^{\mathrm{ideal}}\delta_{\mathrm{prb}}$. We have assumed a parallel orientation of the polarization vectors, i.e., $\mathbf{E}_{\mathrm{prb}}\|\mathbf{E}_{\mathrm{pmp}}\perp\mathbf{v}_i$, as depicted in the lower part of the figure. As expected, all the oscillatory structure visible in the ideal configuration is lost in the experimental configuration. We observe a smooth curve that represents the general behavior of the differential Doppler cross section. The same observation holds for the perpendicular orientation of the polarization vectors: again the oscillatory structure in the ideal configuration is transformed into a smooth curve in the experimental configuration.

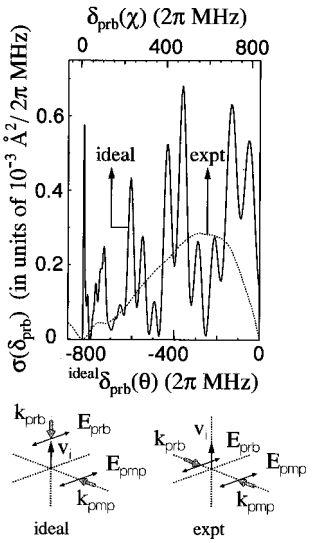

FIG. 22. Calculated results for the differential Doppler cross section for the inelastic $\alpha_5\rightarrow\alpha_4$ transition, both for the ideal pump-probe configuration and the experimental configuration used in the experiments in this paper. Both pump-probe configurations are depicted in the lower part of the figure.

We conclude that in all cases the ideal configuration of the pump- and probe-laser beams, $\mathbf{k}_{\mathrm{pmp}}\perp\mathbf{v}_i$ and $\mathbf{k}_{\mathrm{prb}}\|\mathbf{v}_i$, is to be preferred. However, the experimental configuration used for the experiments presented in this paper does smooth the oscillatory nature but still reveals the general nature of the scattering behavior in many cases. Moreover, in many cases the oscillatory behavior of the inelastic differential cross section is extremely sensitive to minor details of the potentials, leading to the philosophical question if resolving these oscillations really leads to a better understanding of the collision dynamics of these inelastic processes.

IX. CONCLUDING REMARKS

Compared to the two-vector correlation experiments performed by Manders *et al.* [19] and by Boom *et al.* [20], we obtain an enormous amount of additional information from our LIF Doppler probing experiment. As yet, the LIF technique can only be applied to study the $\mathrm{Ne}(3p,\alpha_9\rightarrow\alpha_8)$ transition, with the initial laser-excited state being the upper level of a closed level system. This results in a large increase of the effective life path in this state. In the experiment of elastic collisions of $\mathrm{Ne}(3p,\alpha_7)$ we have shown that competing processes contributing to the LIF signal and the small signals inhibit us to study the elastic four-vector correlation process.

The good agreement between experiment and theory in shape of the differential cross sections and their relative scaling for different laser polarizarion configurations show the power of the model potentials [22–24]. Even up to this level of detail they strongly support the experimentally observed features.

In the Ca-He experiments by Smith *et al.* a more detailed analysis of the experimental results in terms of coherence cross sections is possible, because the gain in signal strength is much longer both due to a ground-state lower level of the Ca and the broad bandwidth of the probe laser. Comparison

with theory, however, is very limited due to the scarce information on potential surfaces for these systems with two valence electrons.

The recent development of bright beams with a 10 000-fold increase in beam flux and ''monochromatic'' velocities [33] offers good prospects for more detailed LIF Doppler experiments on all transitions of the Ne-He system. Elastic collisions as well as other inelastic collisions can be studied when the flux $\dot{N}_{s,i}$ of metastable atoms in the scattering center is increased drastically.

APPENDIX A: LIF SCHEME FOR DETECTING SMALL ANGLE ELASTIC SCATTERING

In this appendix we derive an expression for small angle scattering detected with a Doppler LIF technique. For the configuration where the pump laser is perpendicular to the initial relative velocity $\boldsymbol{v}_i$ (z-axis), the relation between the scattering angle θ and the probing direction (χ,ζ) of Eq. (6) has to be used to derive an expression for the fluorescence signal as a function of the laser detuning $\delta_{\rm prb}$. Basically, the signal is proportional to the nlQ product and we find for the signal

$$S(\delta_{\rm prb}) = C\langle n_{\rm He}\rangle l_s \int_{\chi}^{\chi+\Delta\chi} \int_0^{2\pi} d\zeta\sigma[\theta(\chi,\zeta)]\sin\chi' d\chi', \tag{A1}$$

where C is a scaling constant, $\langle n_{\rm He}\rangle$ is the average He beam density, and l_s is the scattering length of the metastable atoms (≈ 2 mm). The solid angle element is represented by $d\Omega = \sin\chi' d\chi' d\zeta$. The finite χ integration denotes the resonance contition. A more accurate expression for the signal is obtained by integrating over the Lorentz profile $\mathcal{L}(\omega,\gamma_{\rm eff})$ of the transition:

$$S(\delta_{\rm prb}) = C\langle n_2\rangle l_s \int_{-\infty}^{\infty} d\omega \int_0^{2\pi} d\zeta \mathcal{L}(\delta_{\rm prb}-\omega,\gamma_{\rm eff}) \times\sigma[\theta(\chi(\omega),\zeta)], \tag{A2}$$

with $|\delta_{\rm prb}| < \Delta\omega_{\rm max}$. To evaluate the above expression we use Eqs. (5) and (6). We assume that the cross section $\sigma(\omega,\zeta)$ is constant over the width of the Lorentz profile. This approximation reduces the ω integration to unity. We find for the signal

$$S(\delta_{\rm prb}) = C'\langle n_2\rangle l_s \int_0^{2\pi} d\zeta\sigma[\theta(\chi(\delta_{\rm prb}),\zeta)]. \tag{A3}$$

The integral over the azimuthal angle ζ is integrated numerically. When the semiclassical expression for $\theta > \theta_0$ in Eq. (10) is substituted in the integrand, the integral can be approximated by

$$S(\delta_{\rm prb}) \approx C'\langle n_2\rangle l_s(\pi/2+1)[\pi/2-\chi(\delta_{\rm prb})]^{-4/3}. \tag{A4}$$

The exact approximation of the integral with the expression above within 1% in the range $0 < \pi/2-\chi < 0.5$ strongly suggests that a mathematician should be able to derive this expression analytically.

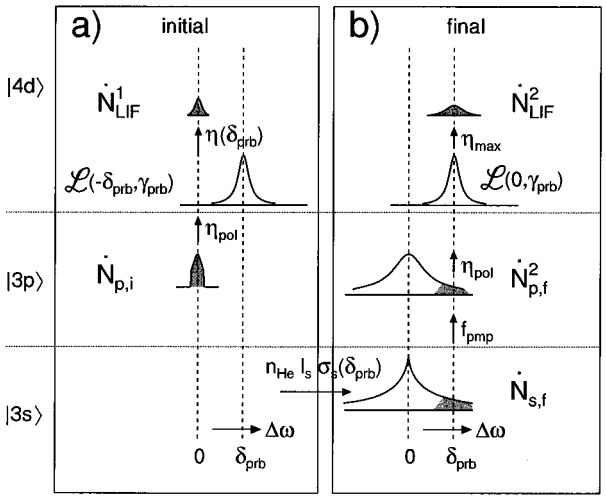

FIG. 23. Schematic representation of competing processes which contribute to the LIF signal of the elastic scattering probing scheme: (a) direct probing of initial $|p\rangle$ states and (b) probing of scattered $|s\rangle$ states.

APPENDIX B: COMPETING PROCESSES IN THE LIF SIGNAL FOR ELASTIC SCATTERING

The two competing processes contributing to the population of the $|d\rangle$ state are graphically represented in Fig. 23 in more detail. The first competing process is the direct excitation of initial $|p\rangle$ to $|d\rangle$ which is depicted in Fig. 23(a). These unscattered $|p\rangle$ states are not resonant with the probe laser. Thus they are converted to LIF photons less efficiently in the off-resonance tail of the line profile as given by

$$\eta(\delta_{\rm prb}) = \eta_{\rm max}\frac{\mathcal{L}(\delta_{\rm prb},\gamma)}{\mathcal{L}(0,\gamma)} = \eta_{\rm max}\frac{1}{1+(2\delta_{\rm prb}/\gamma)^2}, \tag{B1}$$

where γ is the linewidth of the $|p\rangle \rightarrow |d\rangle$ transition and $\mathcal{L}(\Delta\omega,\gamma)$ denotes the Lorentz line shape function. The contribution of the direct excitation can now be written as

$$\dot{N}^1_{\rm LIF} = \eta_{\rm pol}\eta(\delta_{\rm prb})\dot{N}_{p,i}, \tag{B2}$$

with $\dot{N}_{p,i}$ given in Eq. (8).

The second competing process is more complicated and is depicted in Fig. 23(b). Even though the $|s\rangle$ states may be scattered out of resonance, they can still be pumped in the tails of the Lorentz profile. These excited $|p\rangle$ states cannot be distinguished from the actual scattered $|p\rangle$ states that we are interested in. The collision rate $\dot{N}_{s,f}(\delta_{\rm prb})$ for $|s\rangle$ state scattering is obtained thru the effective density length product

$$\dot{N}_{s,f}(\delta_{\rm prb}) = n_{\rm He} l_s \sigma_s(\delta_{\rm prb})\dot{N}_{s,i}, \tag{B3}$$

with $\sigma_s(\delta_{\rm prb})$ being the differential cross section for scattering. Because these scattered $|s\rangle$ states reside in the laser beam for a long time ($\Delta t \approx 1\ \mu{\rm s} \approx 50\tau$), eventually they will be excited by the pump laser

$$\dot{N}^2_{p,f}(\delta_{\rm prb}) = f_{\rm pmp}\dot{N}_{s,f}(\delta_{\rm prb}) = n_{\rm He} l_s \sigma_s(\delta_{\rm prb})\dot{N}_{p,i}, \tag{B4}$$

where we substituted Eq. (8). These excited $|p\rangle$ states contribute to the LIF signal with the same efficiency $\eta_{\max}$ as the scattered $|p\rangle$ states. However, because they have not collided in between the two excitation processes, this undesired contribution may be suppressed by the same factor $\eta_{\rm pol}$ as in Eq. (B2) and can be written as

$$\dot{N}^2_{\rm LIF}(\delta_{\rm prb}) = \eta_{\rm pol} n_{\rm He} l_s \sigma_s(\delta_{\rm prb}) \dot{N}_{p,i}\,. \tag{B5}$$

The ratios $\dot{N}^1_{\rm LIF}/\dot{N}^0_{\rm LIF}$ and $\dot{N}^2_{\rm LIF}/\dot{N}^0_{\rm LIF}$ can now be estimated. The first ratio can be written as

$$\frac{\dot{N}^1_{\rm LIF}}{\dot{N}^0_{\rm LIF}} = \eta_{\rm pol}\,\frac{1}{1+(2\,\delta_{\rm prb}/\gamma)^2}\,\frac{1}{n_{\rm He} l_\tau \sigma_p(\delta_{\rm prb})} \simeq \eta_{\rm pol}\left(\frac{\gamma}{2\,\delta_{\rm prb}}\right)^2 \frac{1}{n_{\rm He} l_\tau \sigma_p(\delta_{\rm prb})}, \tag{B6}$$

where we assume that $\gamma \ll \delta_{\rm prb}$. With $n_{\rm He} \approx 10^{20}\ {\rm m}^{-3}$, $l_\tau \approx 20\ \mu$m, and $\sigma_p(\delta_{\rm prb}) \approx O(5\times 10^{-19}\ {\rm m}^2)$ we find

$$\frac{\dot{N}^1_{\rm LIF}}{\dot{N}^0_{\rm LIF}} \simeq 10^4\,\eta_{\rm pol}\left(\frac{\gamma}{2\,\delta_{\rm prb}}\right)^2. \tag{B7}$$

The second ratio can be approximated by

$$\frac{\dot{N}^2_{\rm LIF}}{\dot{N}^0_{\rm LIF}} \simeq \eta_{\rm pol}\,\frac{l_s \sigma_s(\delta_{\rm prb})}{l_\tau \sigma_p(\delta_{\rm prb})}. \tag{B8}$$

For the two interaction lengths we have, $l_s \approx 2$ mm for the $|s\rangle$ state, and $l_\tau \approx 20\ \mu$m for the $|p\rangle$ state. Assuming that the cross sections σ_s and σ_p are similar in magnitude, this ratio can be estimated with

$$\frac{\dot{N}^2_{\rm LIF}}{\dot{N}^0_{\rm LIF}} \simeq 100\,\eta_{\rm pol}\,. \tag{B9}$$

[1] M. P. I. Manders, J. P. J. Driessen, H. C. W. Beijerinck, and B. J. Verhaar, Phys. Rev. Lett. **57**, 1577 (1986); **57**, 2472 (1986).
[2] J. P. J. Driessen and S. R. Leone, J. Chem. Phys. **96**, 6136 (1992).
[3] E. M. Spain, M. J. Dalberth, P. D. Kleiber, S. R. Leone, S. S. Op de Beek, and J. P. J. Driessen, J. Chem. Phys. **102**, 9522 (1995); **102**, 9532 (1995).
[4] A. G. Suits, H. Hou, H. Floyd Davis, Y. T. Lee, and J.-M. Mestdagh, J. Chem. Phys. **95**, 8178 (1991).
[5] C. J. Smith, J. P. J. Driessen, L. Eno, and S. R. Leone, J. Chem. Phys. **96**, 8212 (1992).
[6] C. J. Smith, E. M. Spain, M. J. Dalberth, S. R. Leone, and J. P. J. Driessen, J. Chem. Soc. Faraday Trans. **89**, 1401 (1993).
[7] R. Düren, E. Hasselbrink, and H. Tisher, Phys. Rev. Lett. **50**, 1983 (1983).
[8] E. E. B. Campbell, H. Hüsler, R. Witte, and I. V. Hertel, Z. Phys. D **16**, 21 (1990).
[9] H. A. Meijer, Z. Phys. D **17**, 257 (1990).
[10] N. Andersen, J. W. Gallagher, and I. V. Hertel, Phys. Rep. **165**, 1 (1988).
[11] G. Nienhuis, Phys. Rev. A **26**, 3137 (1982).
[12] J. Grosser, J. Phys. B **14**, 1449 (1981).
[13] L. J. Kovalenko, S. R. Leone, and J. B. Delos, J. Chem. Phys. **91**, 6948 (1991).
[14] G. C. Schatz, L. J. Kovalenko, and S. R. Leone, J. Chem. Phys. **91**, 6961 (1989).
[15] R. L. Dubs, P. S. Julienne, and F. H. Mies, J. Chem. Phys. **93**, 8784 (1990).
[16] B. Pouilly and M. H. Alexander, Chem. Phys. **145**, 191 (1990).
[17] J. P. J. Driessen and L. Eno, J. Chem. Phys. **97**, 5532 (1992).
[18] R. de Vivie-Riedle, J. P. J. Driessen, and S. R. Leone, J. Chem. Phys. **98**, 2038 (1993).
[19] M. P. I. Manders, W. M. J. Ruyten, F. v. d. Beuken, J. P. J. Driessen, W. J. T. Veugelers, P. H. Kramer, E. J. D. Vredenbregt, W. B. M. van Hoek, G. J. Sandker, H. C. W. Beijerinck, and B. J. Verhaar, J. Chem. Phys. **89**, 4777 (1988).
[20] W. Boom, R. A. M. L. van Galen, B. J. P. Klaver, S. S. Op de Beek, J. T. A. Heier, H. C. W. Beijerinck, and B. J. Verhaar, Phys. Rev. A **51**, 3837 (1995).
[21] T. L. D. Collins, A. J. McCaffery, and M. J. Wynn, Faraday Discuss. Chem. Soc. **91**, 91 (1991).
[22] D. Hennecart and F. Masnou-Seeuws, J. Phys. B **18**, 657 (1985).
[23] D. Hennecart, Ph.D. thesis, Université de Caen, Caen, France, 1982 (unpublished).
[24] H. Kucal, D. Hennecart, and F. Masnou-Seeuws, Chem. Phys. **145**, 163 (1990).
[25] M. J. Verheijen, H. C. W. Beijerinck, L. H. A. M. van Moll, J. P. J. Driessen, and N. F. Verster, J. Phys. E **17**, 904 (1984).
[26] M. P. I. Manders, W. B. M. van Hoek, E. J. D. Vredenbregt, G. J. Sandker, H. C. W. Beijerinck, and B. J. Verhaar, Phys. Rev. A **39**, 4467 (1989).
[27] H. J. L. Megens, *Design of a Continuously Tunable Linewidth Narrowed Diode Laser System* (Eindhoven University of Technology, Eindhoven, 1993).
[28] H. C. W. Beijerinck, P. M. A. van der Kam, W. J. G. Thijssen, and N. F. Verster, Chem. Phys. **45**, 225 (1980).
[29] J. M. Henrichs, H. C. W. Beijerinck, and N. F. Verster, Chem. Phys. **70**, 93 (1982).
[30] S. S. Op de Beek, J. P. J. Driessen, S. J. J. M. F. Kokkelmans, H. C. W. Beijerinck, and B. J. Verhaar, Phys. Rev. A **56**, 2792 (1997).
[31] S. S. Op de Beek, J. P. J. Driessen, H. C. W. Beijerinck, and B. J. Verhaar (unpublished).
[32] S. S. Op de Beek, Master's thesis, Eindhoven University of Technology, The Netherlands, 1992 (unpublished).
[33] M. D. Hoogerland, J. P. J. Driessen, E. J. D. Vredenbregt, H. J. L. Megens, M. P. Schuwer, H. C. W. Beijerinck, and K. A. H. van Leeuwen, Appl. Phys. B **62**, 323 (1996).